
# Supplemental Material

# Supplemental Material to "Synoptic-to-regional scale analysis of rainfall in the Atacama Desert (18°S-26°S) using a long-term simulation with WRF"

Mark Reyers*, Christoph Boehm, Leon Knarr, Yaping Shao, Susanne Crewell

Institute for Geophysics and Meteorology, University of Cologne, Pohligstrasse 3, 50969 Cologne, Germany

*Corresponding author address: M. Reyers, University of Cologne, Institute for Geophysics and Meteorology, Pohligstrasse 3, 50969 Cologne, Germany

E-mail: mreyers@meteo.uni-koeln.de; Tel.: +49 221 4707302; FAX: +49 221 4705161

# Evaluation of WRF-simulated rainfall

For the evaluation of rainfall from the long-term WRF simulation covering the period 1982 to 2017 (Reyers 2018; for details of the model setup see main manuscript) we use rainfall measurements from stations in Northern Chile as provided by the Center for Climate and Resilience Research (CR2: http://explorador.cr2.cl). This observational network is mainly operated by the Chilean National Weather Service (Dirección Meteorológica de Chile), the Chilean Agency of Water (Dirección General de Aguas), and the agrometeorological (AGROMET) weather network of the Ministry of Agriculture. Measurements are available as accumulated daily rainfall. While the observational network is quite dense in Central Chile, measurements are sparse in the Atacama Desert. To overcome the issue of too large data gaps, we decided to select only those stations for the evaluation which cover more than 75% of the period 1982 to 2017. In the target area ranging from 18°S to 26°S in altitudes below 3000 m asl this corresponds to 23 stations (see Fig. S1). For the evaluation, the model grid points which are nearest to the location of the stations are selected, and for these grid points exactly the same dates as available for the respective station are picked out.

Fig. S2 (upper row) depicts the mean annual rainfall at the 23 stations and the corresponding WRF grid points, revealing a good match for the hyper-arid regions and an underestimation towards the Altiplano. However, for the latter the simulated number of rainy days (> 0.1 mm per day) agrees much better to the observations (lower row of Fig. S2), thus indicating that the dry bias is rather due to an underestimation of the rainfall amount within the individual events, while their frequency of occurrence is simulated realistic. Further, maximum daily rainfall occurring in the period 1982-2017 is matched for most stations in the Atacama Desert (middle row in Fig. S2).

Percentile-percentile plots of daily rainfall are shown in Fig. S3. Daily rainfall amounts are underestimated in the WRF simulation at most stations, but this dry bias is rather weak for

the majority of these stations. Largest discrepancies between observed and simulated rainfall are found for the southernmost stations (station numbers 02942001 and 02943001). Mean annual cycles of rainfall (Fig. S4) are mostly reproduced qualitatively well by the WRF model. However, summer rainfall in the Northeast is systematically underestimated (station numbers 01410012, 01502007, 01611001, 01730017, 01740001, and 0175003). As at the same time the simulated number of rainfall days agree much better to observations for these stations (Fig. S5), this underestimation is rather due to the fact that simulated summer rainfall events are less strong than in reality. For station 02112008 (Central Valley), and for stations 02500017 and 02500020 (SE Atacama) the model is not able to reproduce the annual cycle, particularly with respect to the rainfall amount (Fig. S4). A good agreement between simulated and observed yearly cycles is found for the coastal stations 200006 and 01820001 (located between 20°S and 21°S), and for the near-coastal station 02710002 further south.

Finally, the impact of ENSO on rainfall in both the WRF simulation and the observations is analyzed. Fig. S6 show rainfall anomalies for the developing (winter; June-August) and mature phases (summer; December-February) of strong to very strong El Niño and La Niña events in the period 1982-2017 (the selected years are listed in the captions of Fig. S6). In the model, winter El Niño conditions are associated with more rainfall in the southern part of the investigation area (south of 23°S), while slightly less than normal rainfall is simulated for the northern part (Fig. S6a). Very Similar results are found for the observations: Only for the near-coastal stations south of 23°S rainfall anomalies are positive, while no or an only slight negative effect of El Niño is revealed for the other stations. In contrast, during La Niña conditions in winter negative rainfall anomalies occur over almost the entire model domain and most stations (Fig. S6b). Also for the ENSO mature phase in summer the findings for the WRF model agree qualitatively well to what is found for the observations: Strong positive (negative) rainfall anomalies during El Niño (La Niña) are restricted to the northeast, while the impact of ENSO is only marginal in other regions of the investigation area (Fig. S6c and S6d).

When evaluating simulated rainfall in the Atacama Desert, one should keep in mind that the model is employed at the absolute dry limit, such that single events that are not captured well by the model can negatively impact the skill assessment. In that respect, the performance of the WRF model is surprisingly good, and we therefore conclude that the long-term WRF simulation is suitable for rainfall studies in the Atacama Desert, despite the uncovered shortcomings.

## Comparison with radiosonde data

For the grid box corresponding to the location of Antofagasta (see Fig. 1a in the main manuscript) IWV and IWVF values from ERA-Interim are compared to those obtained from radiosonde data. Radiosonde data from the Integrated Global Radiosonde Archive (IGRA; Durre et al., 2006) is used here. For Antofagasta daily soundings are available from the 1950s on, and the radiosonde launch time is mostly 12UTC. However, there are numerous data gaps, particularly in the 1990s. All required variables to derive IWV and IWVF according to Eq. 1 and 2 given in the main manuscript are available from the radiosoundings.

For each of the five composites, Fig. S7 shows radiosonde versus ERA-Interim scatter plots of IWV anomalies, of upper-level IWVF, and of low-level IWVF for the individual rainfall events represented in these composites. A generally good agreement between both datasets is found for the IWV anomalies (Fig. S7, left column). For the majority of the individual rainfall events IWF anomalies at Antofagasta are positive, as expected. Only very few outliers with dry IWV anomalies are found for the radiosonde data, which are not captured by ERA-Interim.

Upper-level IWVF is clearly stronger in ERA-Interim than in the radiosonde data (Fig. S7, middle column). However, for the three winter composites (cl1_MJJA, cl2_JUNE, and cl3_JJA) the scatter plots show that northwesterly IWVF occur during all rainfall events in both

datasets, which agrees well to our results presented in Fig. 4 of the main manuscript. Further, as found for ERA-Interim, also in the radiosonde data low-level IWVF is substantially weaker than the upper-level moisture transport (compare Fig. S7b,e,h to Fig S7c,f,i). These results indicate that our findings and conclusions presented in section 3.2.2 of the main manuscript are reliable. Larger discrepancies between ERA-Interim and radiosonde data are revealed for IWVF of the cl4_JF composite (Fig. S7n and S7o). Hence, for this composite moisture fluxes at the coastal range of the Atacama are probably captured incorrectly by ERA-Interim.

## Lagged composites for the winter rainfall events

Our analysis for the winter rainfall events in SE Atacama (cl2_JUNE) and in North Atacama (cl3_JJA) indicate that positive SST anomalies in the adjacent Pacific ocean are not required to trigger strong winter rainfall in these regions (see Fig. 8d and 8f of the main manuscript). Regarding the findings of other studies (e.g. Bozkurt et al. 2016) this result is somewhat surprising. To better understand the thermo-dynamical processes involved in the winter rainfall events, particularly in SE Atacama and North Atacama, the temporal evolution of IWV and IWVF prior the events are analyzed (Fig. S8, S9, and S10). Five days prior the events (day-5) moist IWV anomalies are located over the Pacific region and Peru north of 20°S in case of cl2_JUNE, and along the coastal zone of Peru in case of cl3_JJA (Fig. S9a and S10a). From day-2 on, a distinct trough is revealed in both composites west of 80°W (Fig. S9d and S10d), and the moist air is transported towards the Atacama Desert at the foreside of these troughs. Two (one) days prior the rainfall events another effect becomes visible for cl2_JUNE (cl3_JJA): due to upward vertical motions within troughs the inversion strength is strongly decreased (see yellow contours in Fig. S9d and S10e). Using water vapor isotopic compositions merged with sounding and satellite data measurements, Galewsky (2018) demonstrates that a weakening of the inversion strength amplifies the water vapor export from the marine boundary

layer into the free troposphere. This moisture is then transported towards Northern Chile when the troughs propagate eastwards. Coinciding with the moisture advection at the foreside of the trough, these processes result in an upper-level IWVF (above 800 hPa) convergence in coastal Northern Chile (Fig. S9f and S10f) and may thus trigger rainfall events in the Atacama Desert. We therefore conclude that the moisture being involved in the rainfall events of cl2_JUNE and cl3_JJA likely originates from tropical continental areas and the tropical Southeast Pacific, as well as from the remote subtropical Pacific, and that positive SST anomalies in the adjacent ocean are thus not necessarily required to trigger these events. For the winter rainfall events in South Atacama (cl1_MJJA) similar thermo-dynamical processes are observed (Fig. S8). As these events are associated with positive SST anomalies (see Fig. 8b of the main manuscript) and affect a broader area and yield higher precipitation amounts (see Fig. 3a of the main manuscript) when compared to cl2_JUNE and cl3_JJA, an impact of SST should be taken into account.

# References

Bozkurt, D., R. Rondanelli, R. Garreaud, and A. Arriagada, 2016: Impact of Warmer Eastern Tropical Pacific SST on the March 2015 Atacama Floods. *Mon. Wea. Rev.*, **144**, 4441-4460. doi:10.1175/MWR-D-16-0041.1

Durre, I., R. S. Vose, and D. B. Wuertz, 2006: Overview of the Integrated Global Radiosonde Archive. *J. Climate*, **19**, 53-68.

Galewsky, J., 2018: Relationships between inversion strength, lower-tropospheric moistening, and low-cloud fraction in the subtropical Southeast Pacific derived from stable isotopologues of water vapor. *Geophys. Res. Lett*., **45**, 7701-7710. doi:10.1029/2018GL078953

[dataset] Reyers, M., 2018: WRF Output daily accumulated total precipitation 10km resolution Atacama. CRC1211 Database (CRC1211DB). doi:10.5880/CRC1211DB.20

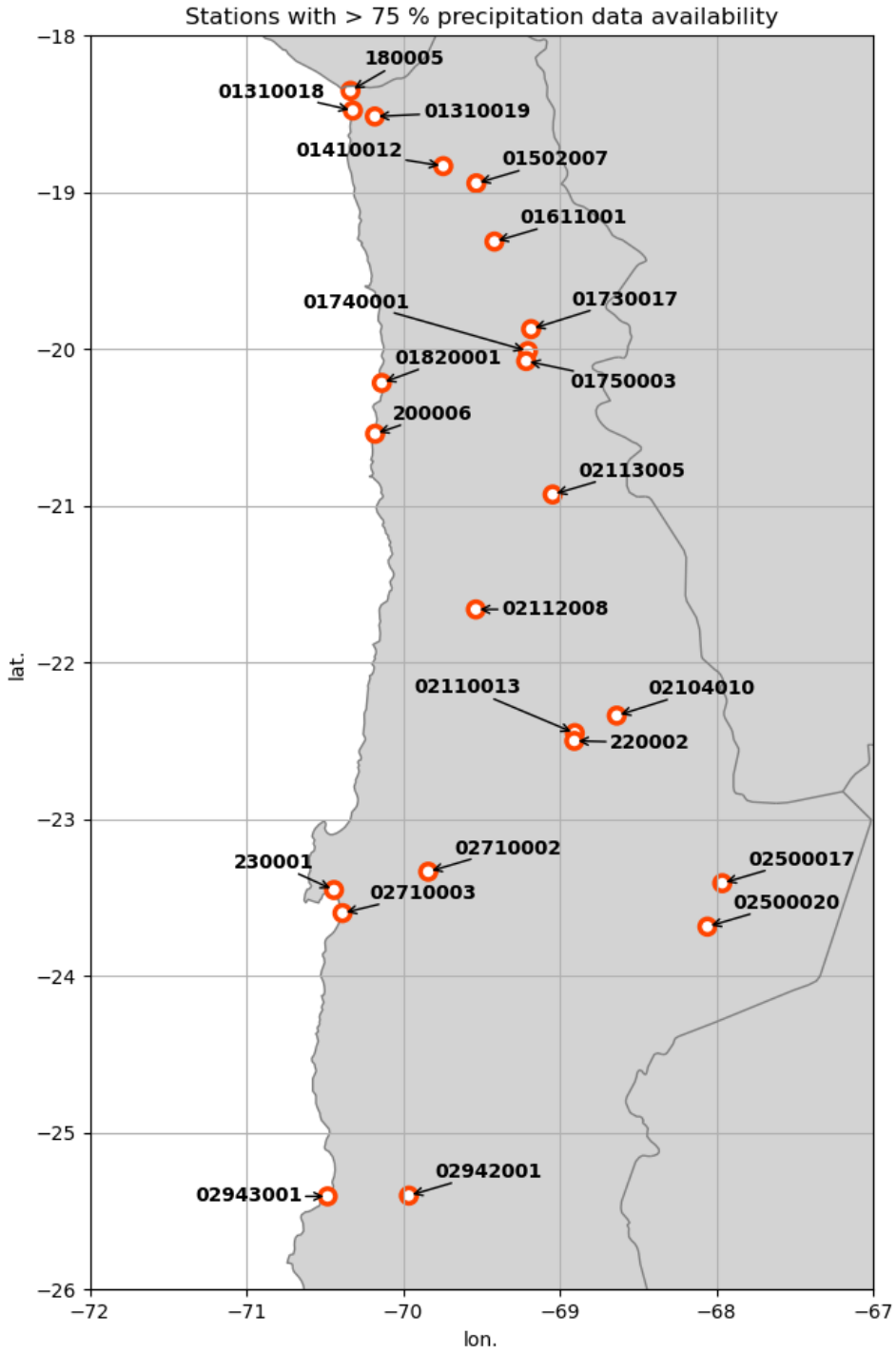


Fig. S1: Location and station number of the CR2 stations in Northern Chile with more than 75% data availability in the period 1982-2017.

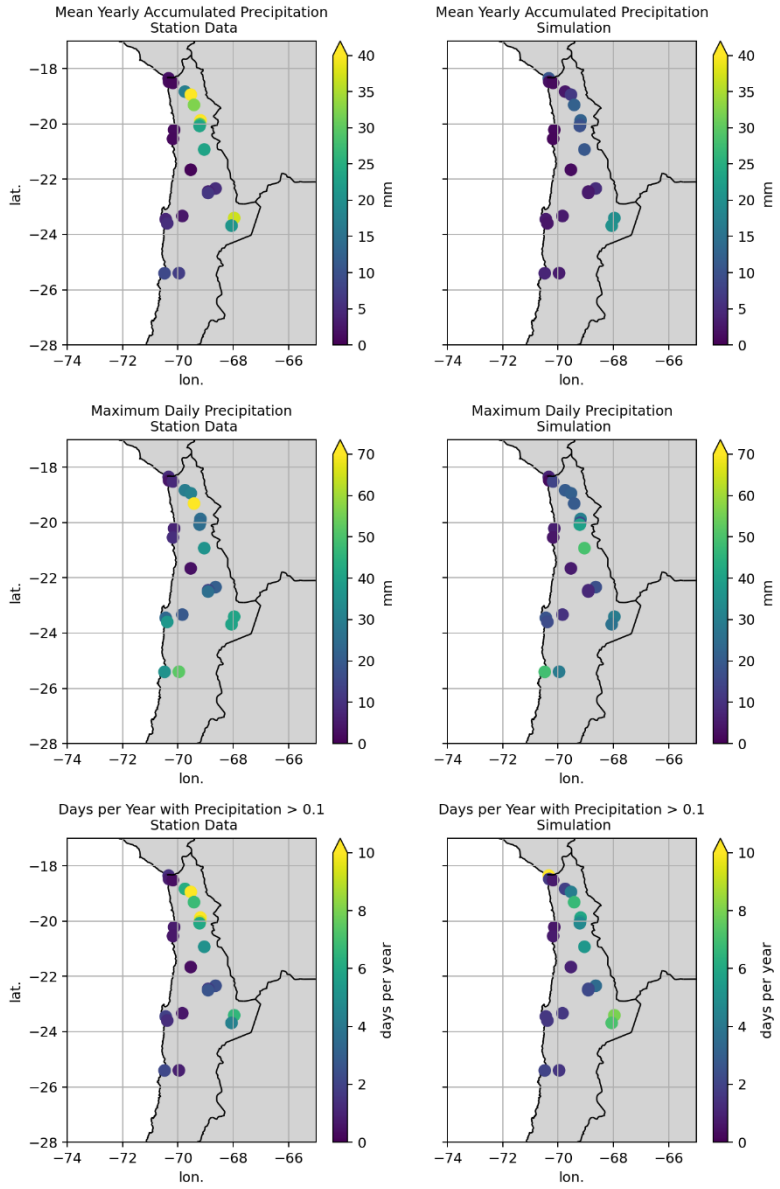


Fig. S2: Mean annual rainfall (upper row, in mm per year), maximum daily precipitation (middle row, in mm per day), and mean number of days with rainfall of more than 0.1 mm per day (lower row, in days per year) in observations (left column) and at the corresponding WRF grid points (right column) at the stations shown in Fig. S1.

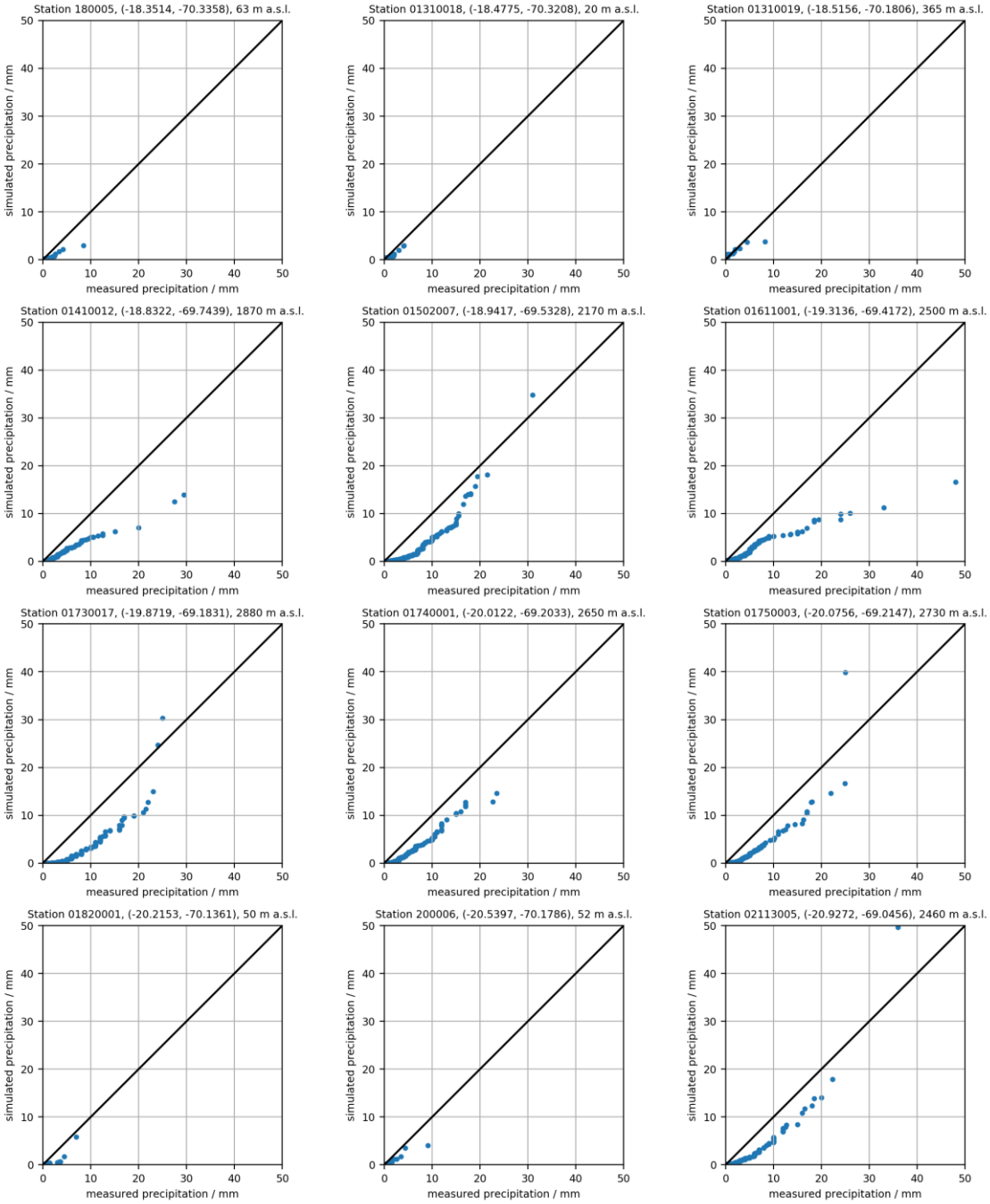


Fig. S3: Percentile-percentile plots of simulated versus observed daily rainfall (in mm per day) at the stations shown in Fig. S1. Panels are arranged from North (upper left) to South (lower right).

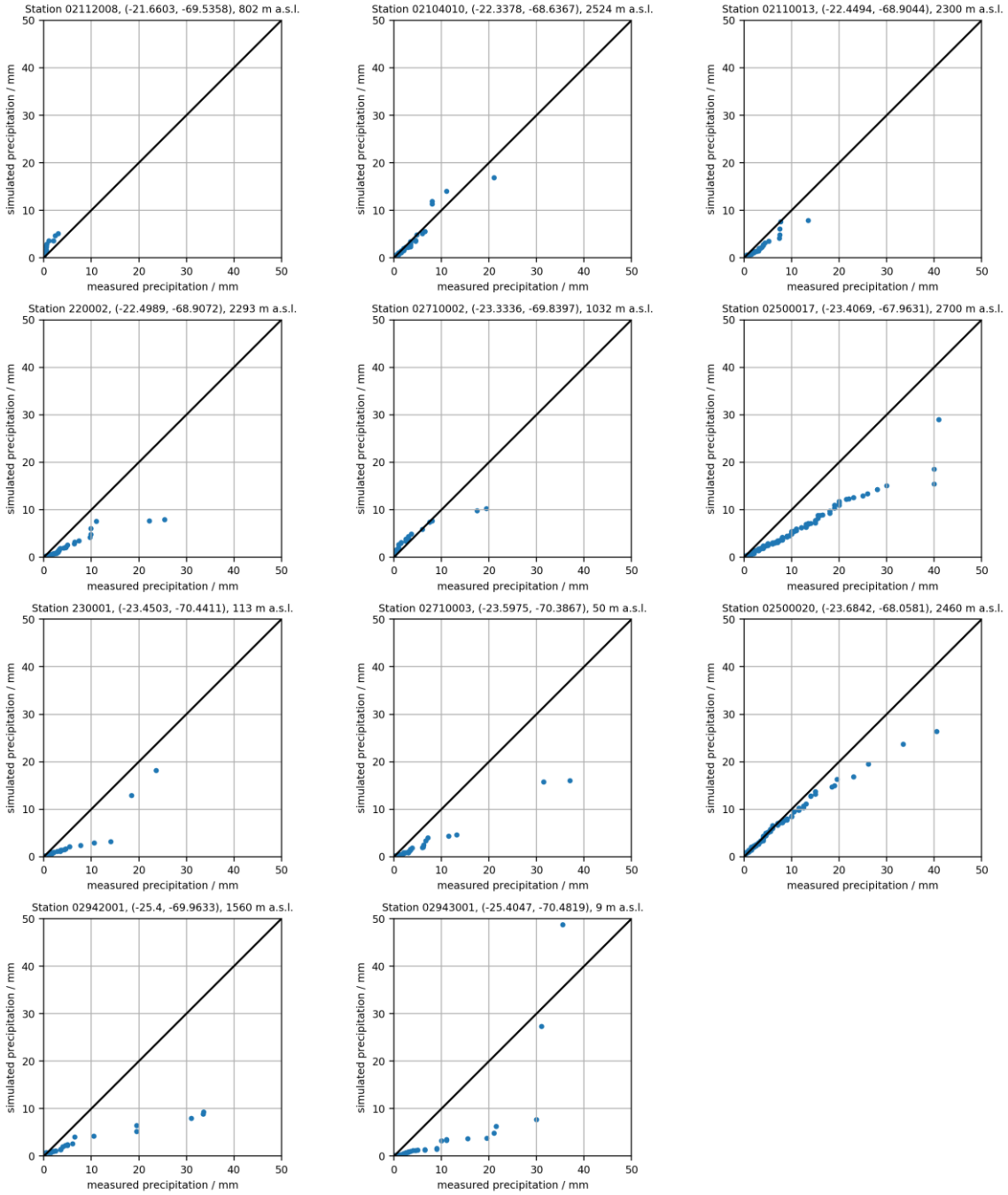


Fig. S3 continued.

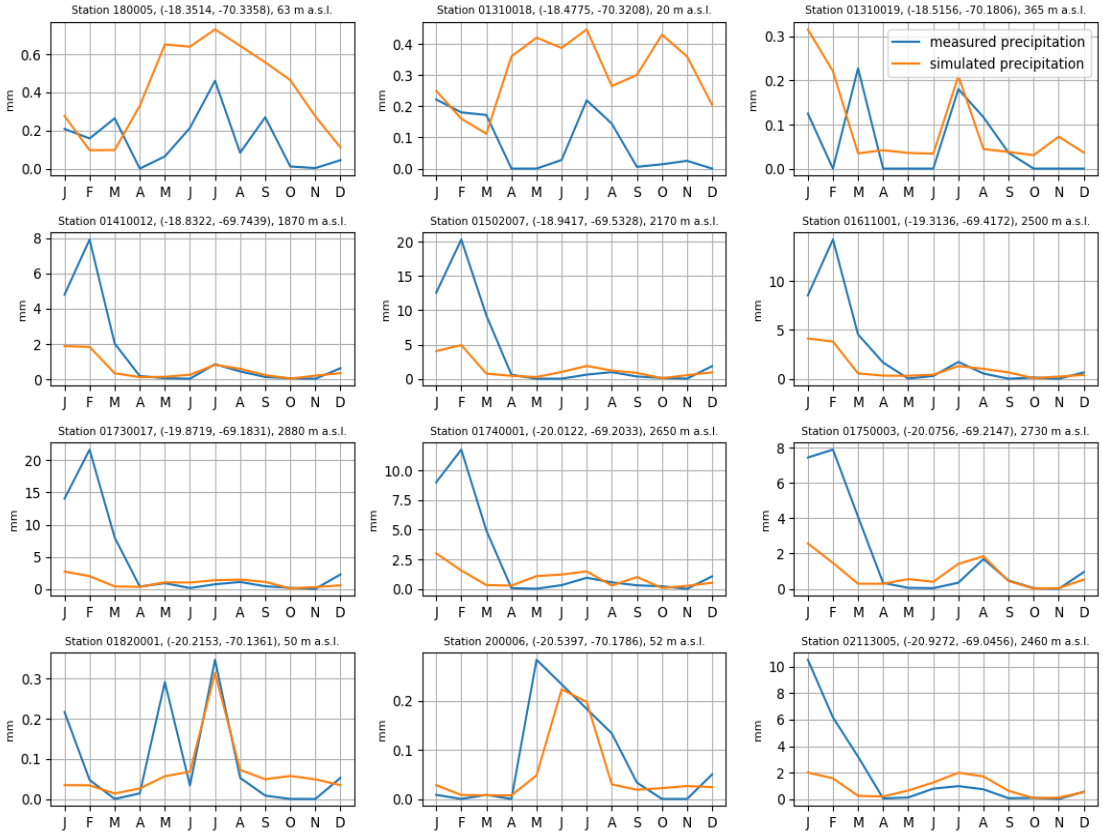


Fig. S4: Mean annual cycles of rainfall (in mm per month) as obtained by the WRF-model (orange) and from observations (blue) at the stations shown in Fig. S1. Panels are arranged from North (upper left) to South (lower right).

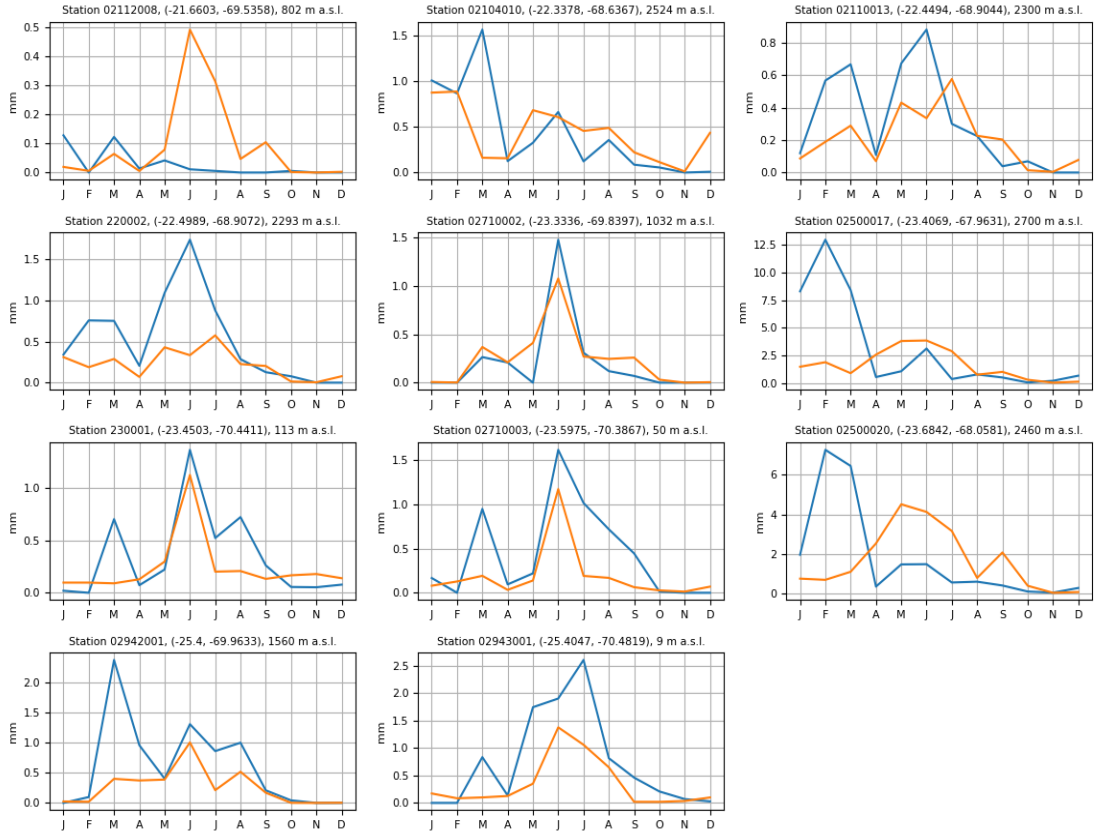


Fig. S4 continued.

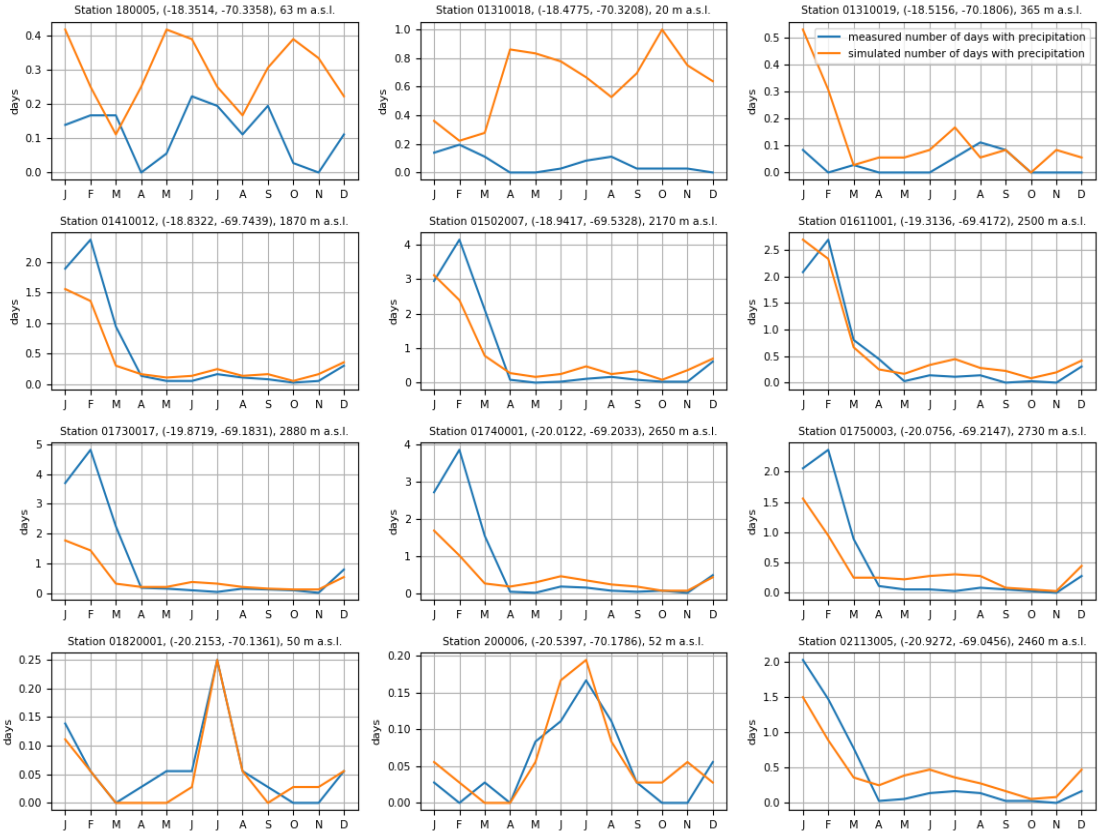


Fig. S5: Mean annual cycles of the number of days with rainfall > 0.1 mm (in days per month) as obtained by the WRF-model (orange) and from observations (blue) at the stations shown in Fig. S1. Panels are arranged from North (upper left) to South (lower right).

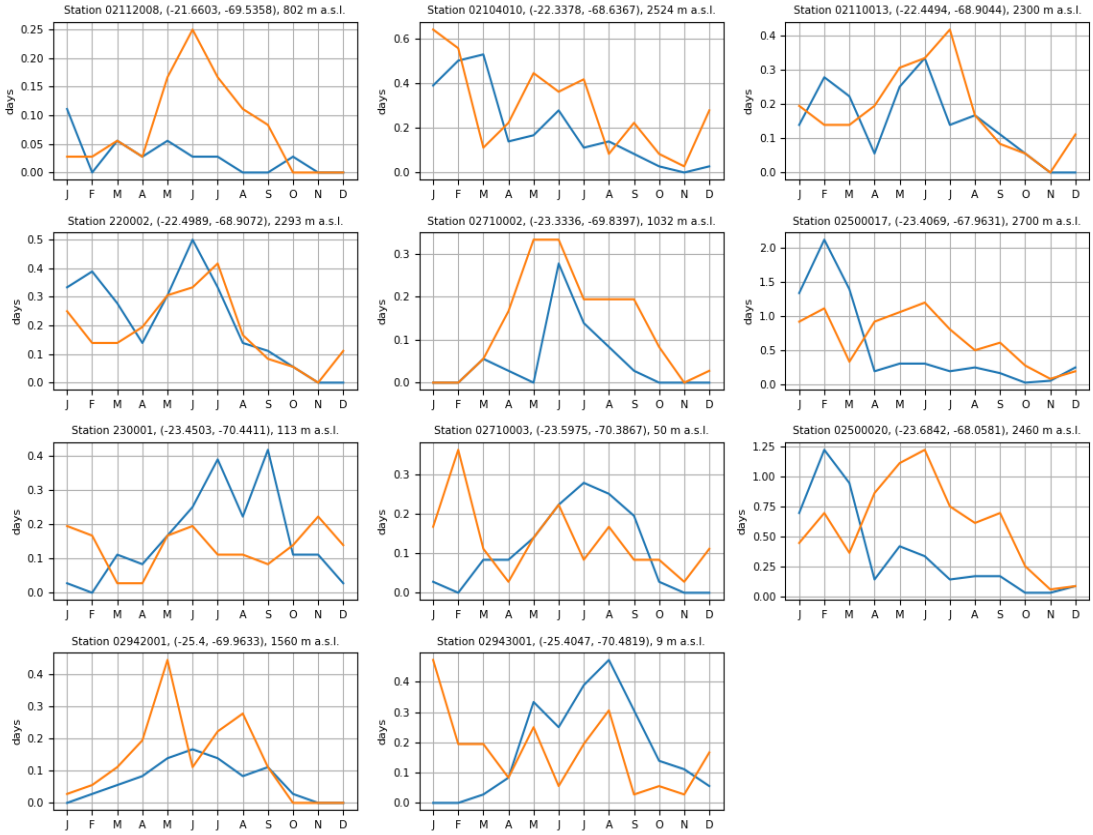


Fig. S5 continued.

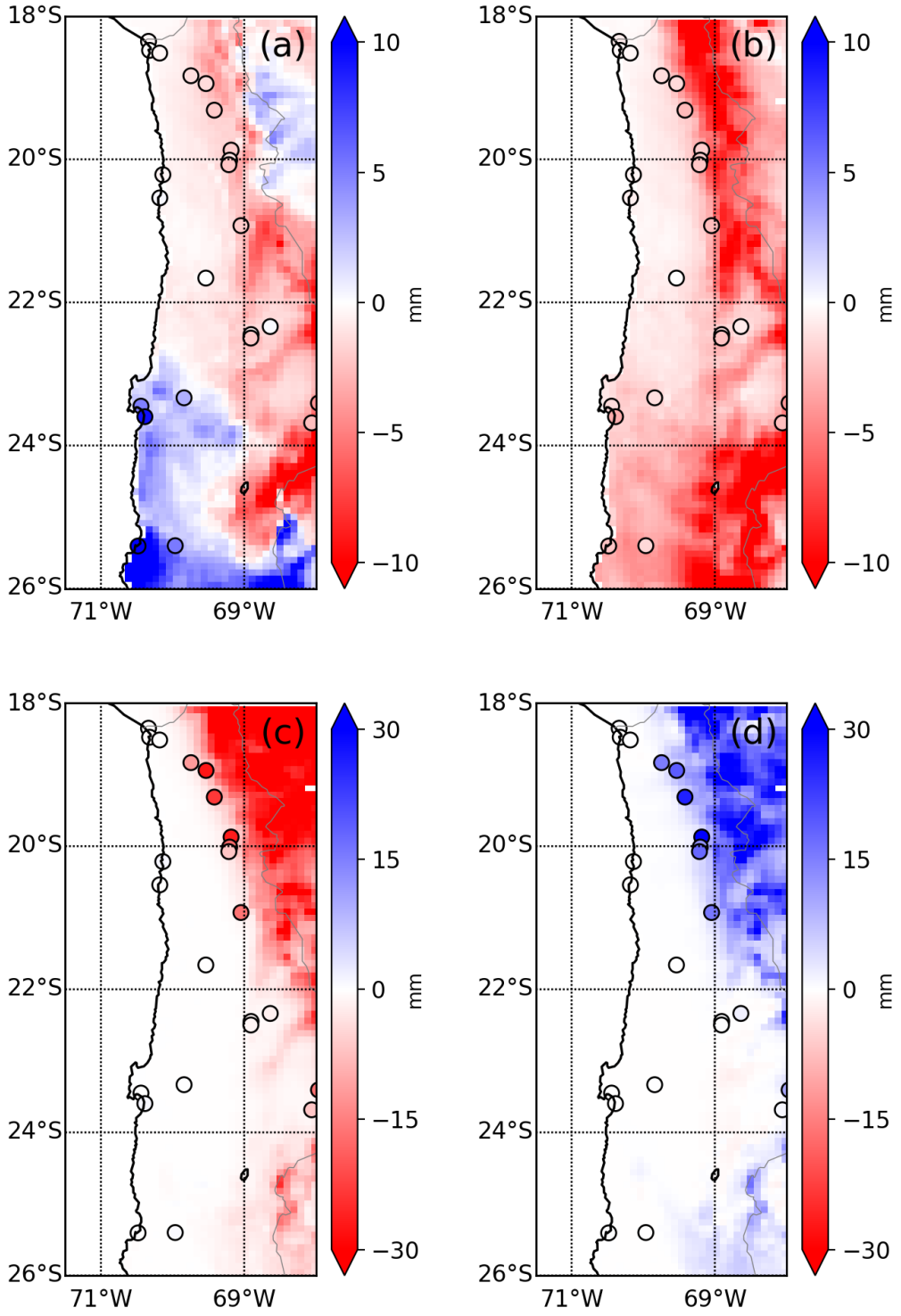


Fig. S6: Simulated (shading) and observed (colored circles) rainfall anomalies (in mm per season) in the developing (upper row; June-August) and mature phases (lower row; December-February) during (a,c) El Niño years (1982/1983, 1987/1988, 1991/1992, 1997/1998, 2015/2016) and (b,d) La Niña years (1988/1989, 1998/1999, 1999/2000, 2007/2008, 2010/2011).

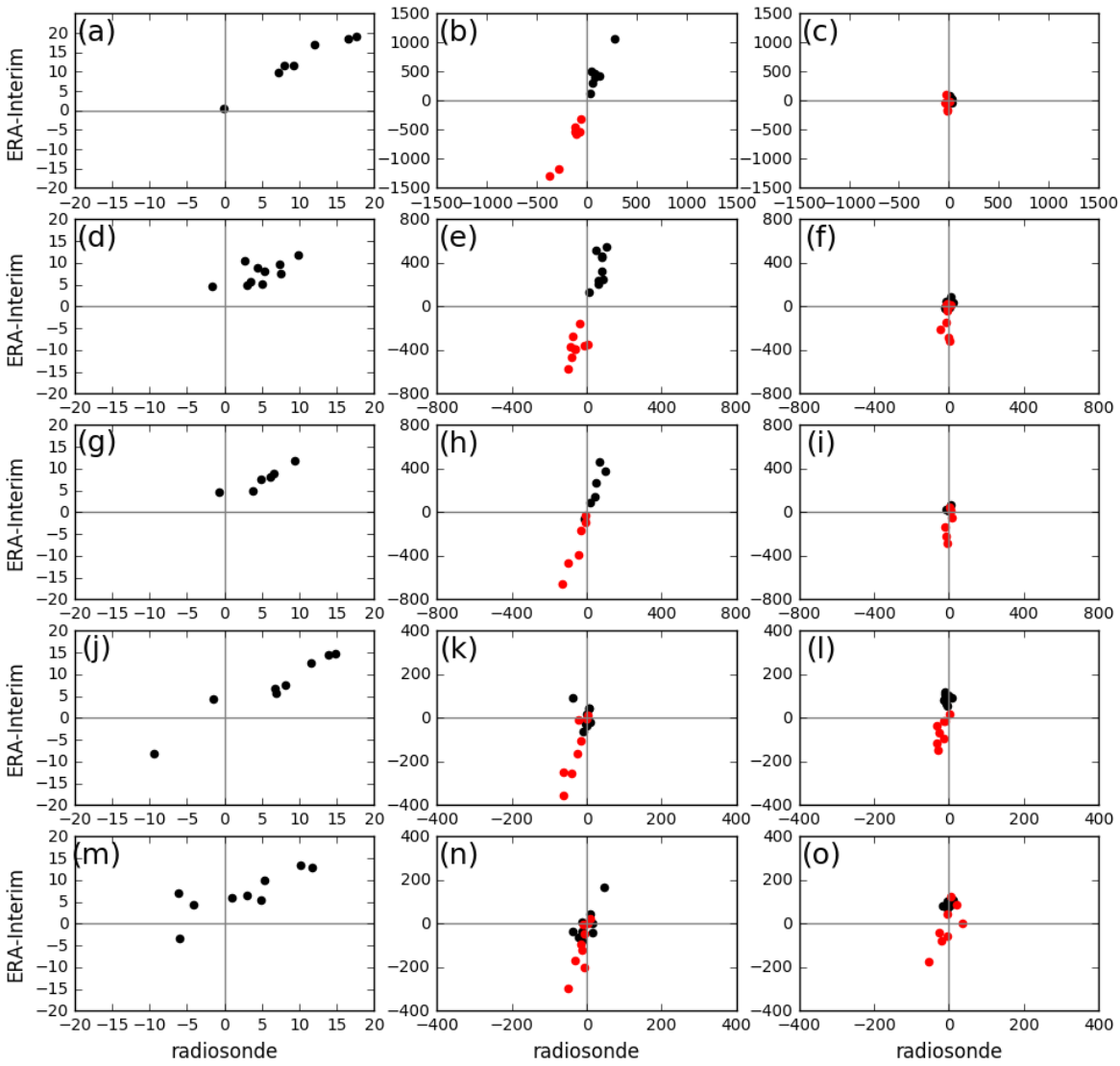


Fig. S7: Scatter plots of IWV anomalies (left column, in in $kg \cdot m^{-2}$), upper-level IWVF components (middle column, in $kg \cdot m^{-1} \cdot s^{-1}$; black/red dots for the u/v-component), and low-level IWVF components (right column, in $kg \cdot m^{-1} \cdot s^{-1}$; black/red dots for the u/v-component) for radiosonde data at Antofagasta versus ERA-Interim (at grid box which is nearest to the location of Antofagasta) for the individual rainfall events of cl1_MJJA, cl2_JUNE, cl3_JJA, cl3_JF, and cl4_JF (from top to bottom).

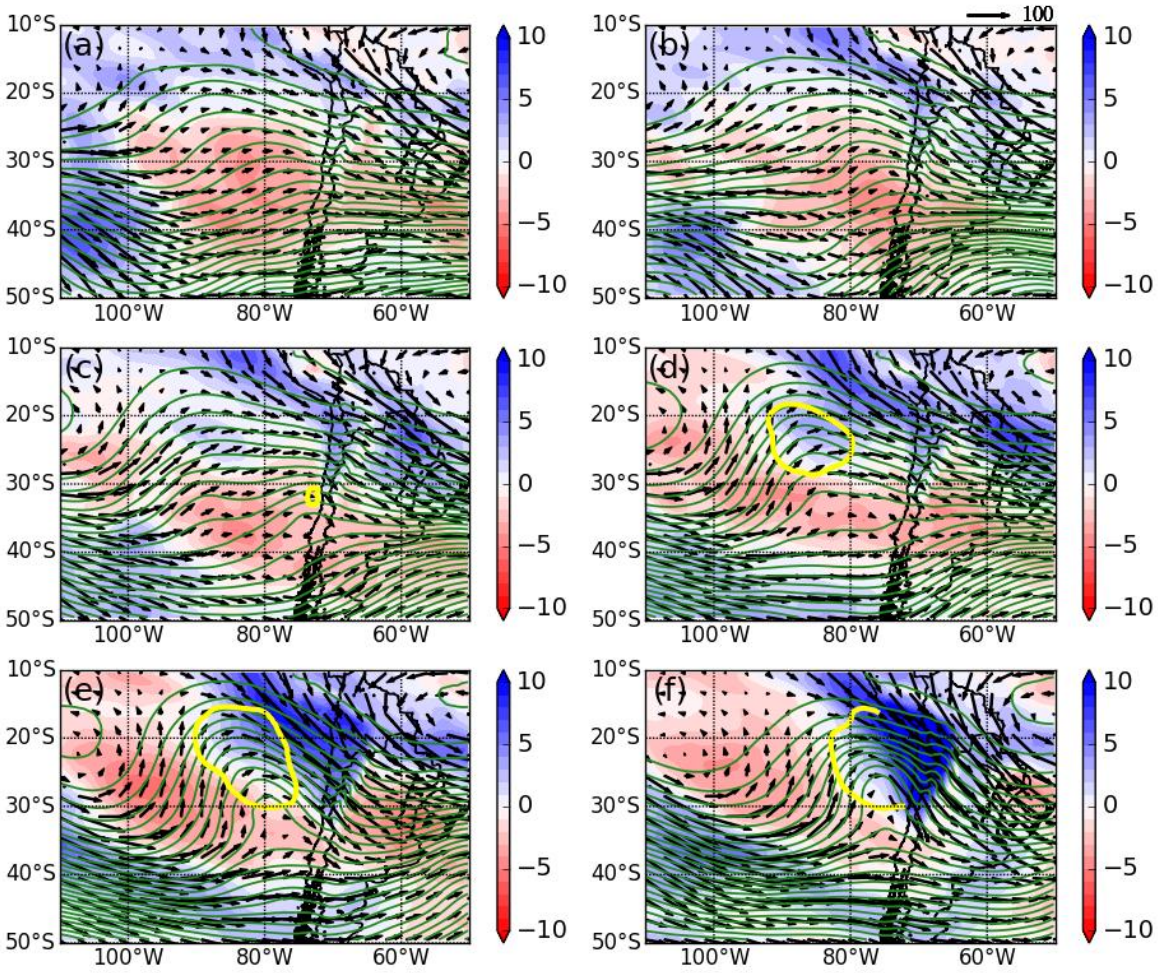


Fig. S8: Composite means of z500 (green contours, every 20 gpm) and upper-level IWVF (black arrows, in $kg \cdot m^{-1} \cdot s^{-1}$), and composite anomalies of IWV (shading, in $kg \cdot m^{-2}$) and inversion strength (bold yellow line shows the -4 K isoline) from ERA-Interim for cl1_MJJA at (a)-(e) five days to one day before the selected events, and (f) at the day of the rainfall events. The IWV and inversion strength anomalies are given relative to the climatology over the respective season.

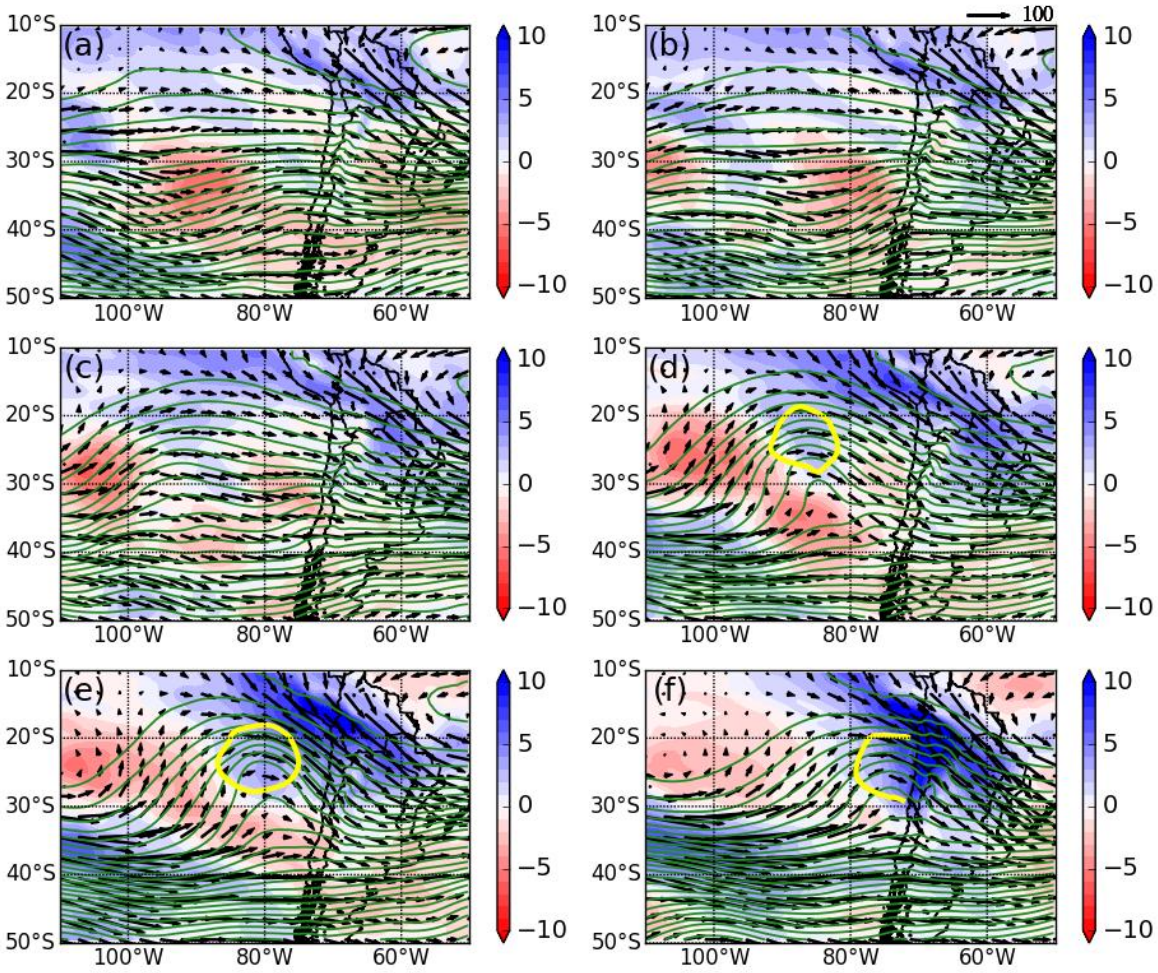


Fig. S9: As Fig. S8, but for cl2_JUNE.

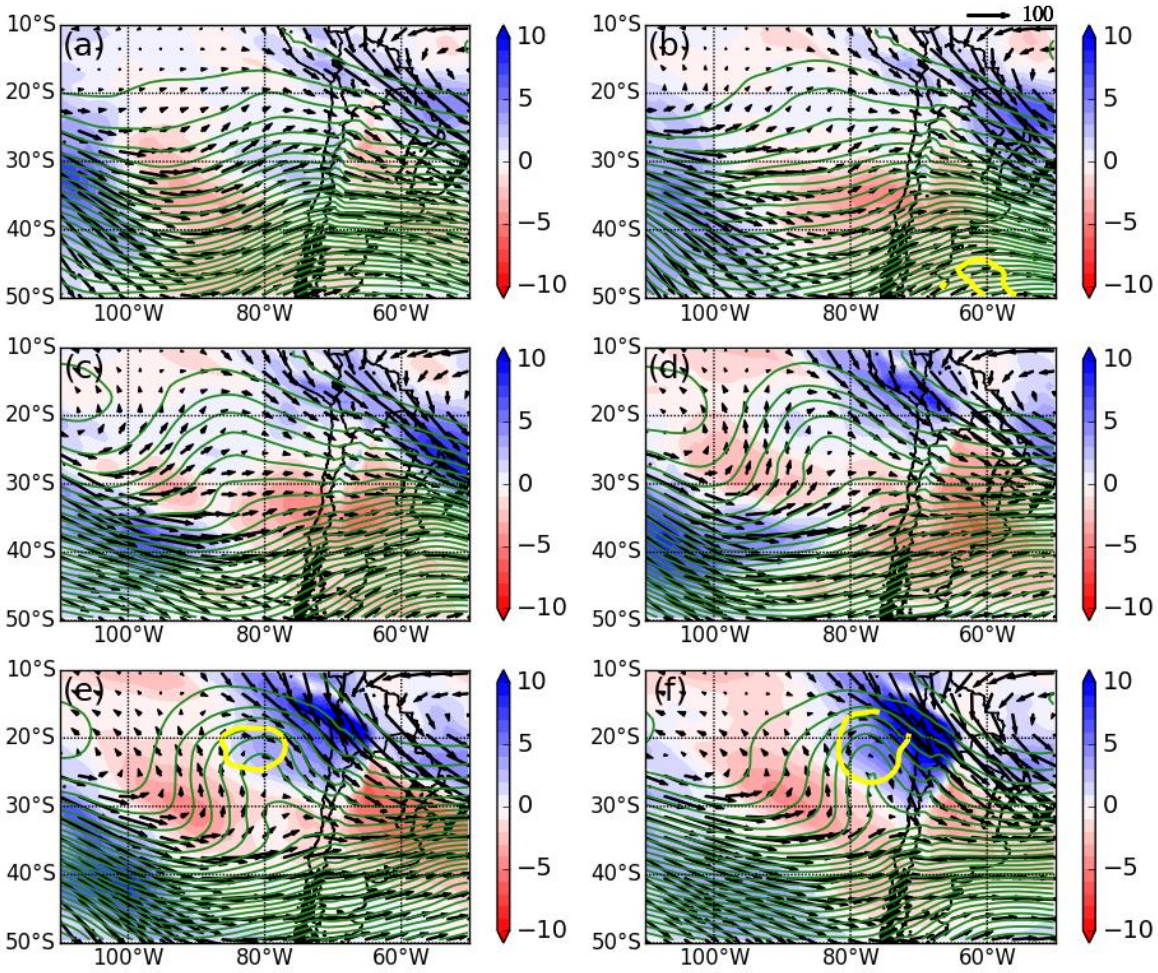


Fig. S10: As Fig. S8, but for cl3_JJA.